Video-rate optical flow corrected intraoperative functional fluorescence imaging

Koch, Maximilian; Glatz, Juergen; Ermolayev, Vladimir; de Vries, Elisabeth G. E.; van Dam, Gooitzen M.; Englmeier, Karl-Hans; Ntziachristos, Vasilis

Published in:
Journal of Biomedical Optics

DOI:
10.1117/1.JBO.19.4.046012

Publication date:
2014

Journal of Biomedical Optics

SPIEDigitalLibrary.org/jbo

Fluorescence lifetime imaging and reflectance confocal microscopy for multiscale imaging of oral precancer

Joey M. Jabbour
Shuna Cheng
Bilal H. Malik
Rodrigo Cuenca
Javier A. Jo
John Wright
Yi-Shing Lisa Cheng
Kristen C. Maitland

Fluorescence lifetime imaging and reflectance confocal microscopy for multiscale imaging of oral precancer

Joey M. Jabbour,[a] Shuna Cheng,[a] Bilal H. Malik,[a] Rodrigo Cuenca,[a] Javier A. Jo,[a] John Wright,[b] Yi-Shing Lisa Cheng,[b] and Kristen C. Maitland[a]

[a]Texas A&M University, Department of Biomedical Engineering, 5045 Emerging Technologies Building, 3120 TAMU, College Station, Texas 77843
[b]Texas A&M University Health Science Center—Baylor College of Dentistry, Department of Diagnostic Sciences, 3302 Gaston Avenue, Dallas, Texas 75246

Abstract. Optical imaging techniques using a variety of contrast mechanisms are under evaluation for early detection of epithelial precancer; however, tradeoffs in field of view (FOV) and resolution may limit their application. Therefore, we present a multiscale multimodal optical imaging system combining macroscopic biochemical imaging of fluorescence lifetime imaging (FLIM) with subcellular morphologic imaging of reflectance confocal microscopy (RCM). The FLIM module images a 16×16 mm^2 tissue area with 62.5 μm lateral and 320 ps temporal resolution to guide cellular imaging of suspicious regions. Subsequently, coregistered RCM images are acquired at 7 Hz with 400 μm diameter FOV, <1 μm lateral and 3.5 μm axial resolution. FLIM-RCM imaging was performed on a tissue phantom, normal porcine buccal mucosa, and a hamster cheek pouch model of oral carcinogenesis. While FLIM is sensitive to biochemical and macroscopic architectural changes in tissue, RCM provides images of cell nuclear morphology, all key indicators of precancer progression. [DOI: 10.1117/1.JBO.18.4.046012]

Keywords: confocal microscopy; fluorescence lifetime imaging; multimodal imaging; cancer; tissue phantom; *in vivo* imaging.

Paper 12824RR received Dec. 27, 2012; revised manuscript received Mar. 19, 2013; accepted for publication Mar. 22, 2013; published online Apr. 17, 2013.

1 Introduction

Eighty to ninety percent of all cancers originate in epithelial tissues, such as in the oral cavity, cervix, esophagus, and colon.[1] If detected at an early stage, the morbidity and mortality of this disease may be greatly reduced.[2] Due to the superficial location of many of these tissues, optical imaging techniques have shown considerable promise towards early detection of pathological changes and are being explored for noninvasive detection of early cancer.[3–11] Optical techniques can noninvasively probe biochemical and/or morphological changes associated with precancer progression, and are particularly amenable to epithelial tissues accessible by rigid or flexible endoscopes.[12] Additionally, optical techniques are applicable on a wide range of scales, from subcellular to organ level imaging. However, imaging systems are typically designed to either have a macroscopic view, sacrificing spatial resolution, or to have high resolution within a limited field of view (FOV). The ideal optical diagnostic would have high sensitivity macroscopic surveillance guiding high resolution and high specificity imaging for diagnosis.

High resolution imaging, such as confocal or nonlinear microscopy, provides information about tissue architecture and cellular morphology similar to histology.[7,13] Reflectance confocal microscopy (RCM) uses spatial filtering through a confocal pinhole to remove out of focus scattered light, generating high resolution "optical sections" of tissue.[14] The greatest source of RCM image contrast in the epithelium is variation in tissue refractive index, for example in the cell nuclei compared to the surrounding cytoplasm.[15] This enables visualization of cell nuclei and quantification of features such as the nuclear-to-cytoplasmic ratio. The nuclear-to-cytoplasmic ratio is one of the morphological features for diagnosis of oral epithelial dysplasia and oral squamous cell carcinoma.[16] Other morphological/cytological features include large and prominent nucleoli, increased mitotic activity, abnormal mitoses, and cellular and nuclear pleomorphism.[17] RCM has been demonstrated to distinguish these morphological changes between normal, precancerous, and cancerous oral tissue;[18,19] however, RCM typically has a limited FOV and requires guidance on the macroscale. Guidance may be provided by visual inspection, which is highly dependent on the clinical experience of the examiner.[10] Even for experienced clinicians, some early oral malignant lesions may be indistinguishable from benign lesions and premalignant lesions can be quite large and heterogeneous, complicating identification of the most severe site of disease for measurement. In gastrointestinal applications, endomicroscopy guidance may be provided using traditional white light endoscopy, fluorescence endoscopy, or other contrast enhanced endoscopy techniques.[12,20] The combination of large FOV imaging for macroscopic surveillance with high resolution imaging or point measurement techniques has the potential to improve diagnosis and diagnostic yield by guiding the effective point sampling technique to the site with the most advanced state of disease within a lesion or the oral cavity.[11,21–23]

Wide-field autofluorescence imaging instruments are commercially available for clinical oral cancer detection;[24,25] however, while they may be sensitive to biochemical changes in the tissue, differentiation of (pre)malignant from benign lesions remains a challenge.[26,27] The primary endogenous fluorophores

Address all correspondence to: Kristen C. Maitland, Texas A&M University, Department of Biomedical Engineering, 5045 Emerging Technologies Building, 3120 TAMU, College Station, Texas 77843. Tel: (979) 845-1864; Fax: (979) 845-4450; E-mail: kmaitland@tamu.edu

of interest in epithelial precancer progression are collagen cross-links in the stroma and metabolic cofactors nicotinamide adenine dinucleotide (NADH) and flavin adenine dinucleotide (FAD) in epithelial cells. Increased cellular metabolism in epithelial dysplasia results in an increase in NADH and FAD fluorescence signal; conversely, in inflammation, the epithelial cell fluorescence decreases slightly.[28] However, the overall tissue fluorescence from abnormal lesions generally decreases due to the more substantial decrease in stromal collagen fluorescence with inflammation and dysplasia. The loss of collagen fluorescence signal is attributed to the breakdown of collagen cross-links, infiltration of lymphocytes in the stroma, and increased epithelial thickness and scattering.[28,29] Because the overall fluorescence signal is dominated by stromal fluorescence which decreases with both inflammation and dysplasia, fluorescence from NADH and collagen need to be separated in order to differentiate between benign and precancerous lesions. The overlapping spectral properties of NADH and collagen complicate analysis based solely on fluorescence intensity. Optical sectioning techniques, such as multiphoton microscopy, can spatially separate epithelial from stromal signal; however, slow acquisition time for three-dimensional scanning and small FOV result in similar disadvantages to RCM for screening of large organs, and with a higher system complexity and cost. The addition of lifetime measurements in large-FOV fluorescence lifetime imaging (FLIM) is another option to decouple contributions from different fluorophores, potentially providing a more accurate analysis of the metabolic activity in precancerous tissue over fluorescence intensity alone.[30–32] Moreover, the fluorescence lifetime is sensitive to the local microenvironment, serving as an additional indicator towards characterizing malignant transformation, and is less sensitive to intensity artifacts such as photo-bleaching and excitation power. The multispectral FLIM system presented here has the ability to simultaneously collect fluorescence intensity and lifetime images in three different channels corresponding to the peak emission wavelengths of NADH, FAD, and collagen, providing multiple biochemical indicators to characterize the specimen.

In this paper, we present a dual modality imaging system to detect both biochemical and morphological changes that are associated with oral precancer progression. Specifically, the integrated system uses FLIM to provide real-time wide-field, low spatial resolution images of the biochemical makeup of the specimen. These images then serve as a guide to direct RCM imaging to suspicious sites within the tissue. Coregistered RCM facilitates morphological imaging of the subcellular structure of the epithelium with small FOV but very high spatial resolution in three dimensions. Here, we demonstrate the multiscale biochemical and morphological imaging capability of this integrated system using a tissue phantom, normal porcine oral mucosa *ex vivo*, and premalignant hamster oral mucosa *in vivo*.

2 Methodology

2.1 *Multiscale Imaging System*

The multimodal optical system was designed to probe the biochemical properties of tissue on a macroscopic scale and the cellular morphology with high resolution. Therefore, large-field FLIM and high-resolution RCM subsystems are placed adjacently with a common sample translation stage for coregistration of images. A detailed schematic of our integrated system is shown in Fig. 1.

The wide-field FLIM subsystem was built following a previously reported multispectral time-domain scanning implementation.[33] It used an ultraviolet (UV) frequency-tripled Q-switched ND:YAG laser (355 nm, 1 ns pulse-width, 100 kHz maximum repetition rate, AOT-YVO-100QSP/MOPA, Advanced Optical Technology, Essex, United Kingdom) for excitation. The laser light was coupled into a multimode fiber with a 50 μm diameter high –OH silica core (FVP050055065, Polymicro Technologies, Phoenix, Arizona). The fiber output was collimated and then reflected by a dichroic mirror (DM1, NC176741-z355rdc, $T > 95\%$ for 380 to 800 nm, Chroma Technology Corporation, Bellows Falls, Vermont) to a pair of close-coupled galvanometer mirrors (6200HM40, Cambridge Technology, Lexington, Massachusetts) for two-dimensional raster scanning. A UV-to-NIR corrected triplet (NT64-837, Edmunds Optics, Barrington, New Jersey) with a focal length of 45 mm and effective numerical aperture (NA) of 0.06 was used to focus light onto the sample. The fluorescence emission was collected by the same triplet before being separated from the excitation light by DM1 and coupled into a multimode fiber with a 200 μm core diameter (BFL22-200, Thorlabs, Newton, New

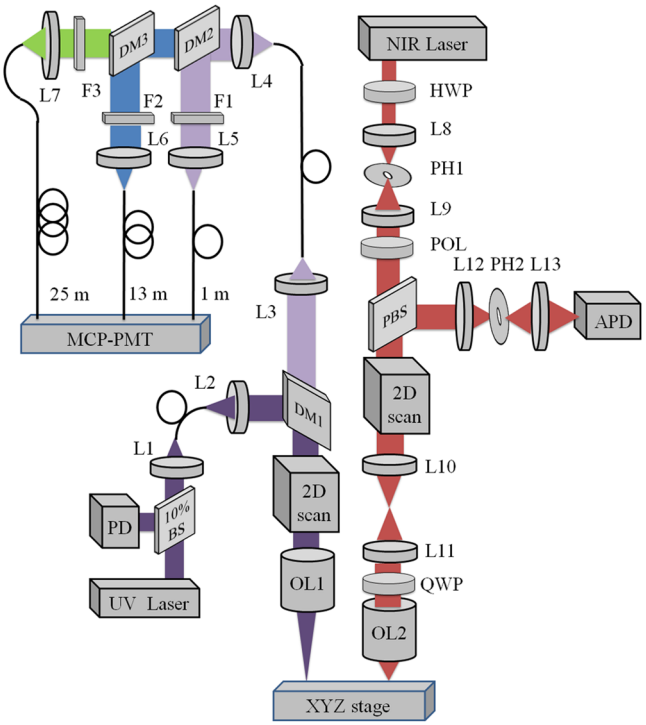

Fig. 1 Schematic of the combined fluorescence lifetime imaging-reflectance confocal microscopy (FLIM-RCM) system. Left: The FLIM module uses a ultraviolet (UV) pulsed laser, two galvanometer scanning mirrors, and a 45 mm focal length triplet lens (OL1). Three emission bands centered at 390 nm for collagen, 452 nm for nicotinamide adenine dinucleotide (NADH), and >500 nm for flavin adenine dinucleotide (FAD) are spectrally separated by dichroic mirrors (DM) and filters (F), temporally separated by three multimode fibers of 1, 13, and 25 m length, and detected by a single gated micro-channel plate photomultiplier tube (MCP-PMT). A 10% beamsplitter (BS) and photodiode (PD) provide the trigger for data acquisition. Right: the RCM module uses a NIR laser, resonant and galvanometer scanning mirrors, and 1.0 NA objective lens (OL2). Spatial filters [lenses (L) and pinholes (PH)] are used in confocal illumination and detection, and signal is detected by an avalanche photodiode (APD). A half wave plate (HWP) and polarizer (POL) are used to control power, and a quarter wave plate (QWP) and polarizing beamsplitter (PBS) reduce specular reflection. An XYZ translation stage coregisters FLIM and RCM images.

Jersey). The fiber output was collimated and separated into three spectral bands using two dichroic mirrors (DM2, LM01-427-25, $T > 95\%$ for 439 to 647 nm, and DM3, FF484-Fdi01, $T > 95\%$ for 492 to 950 nm, Semrock, Rochester, New York). The emission collection spectral bands were further specified by two bandpass filters (FF01-390/40, FF01-452/45, Semrock) and a long pass filter (FF01-496, Semrock) selected based on emission spectra of the three endogenous fluorophores of interest: collagen (F1: 390 ± 20 nm), NADH (F2: 452 ± 22.5 nm) and FAD (F3: >500 nm). The three emission bands were then temporally separated using three multimode fibers with lengths of 1, 13, and 25 m (BFL22-200, Thorlabs) providing a time delay of 60 ns between two consecutive spectral bands to allow measurement of the fluorescence lifetime in the three spectral bands with a single detector. The outputs of the three fibers are then detected by a high-speed (180 ps rise time, 90 ps TTS) micro-channel plate photomultiplier tube (MCP-PMT, R5916U-50, Hamamatsu, Bridgewater, New Jersey), amplified by a preamplifier (C5594-12, Hamamatsu) and sampled by a digitizer at 6.25 GHz (PXIe-5185, National Instruments, Austin, Texas) using custom software programmed in LabVIEW (National Instruments). The FLIM data was then processed in MATLAB (Mathworks, Natick, Massachusetts). For each sample, three normalized intensity maps (I_{1n}, I_{2n}, and I_{3n}) and three average lifetime maps (τ_1, τ_2, and τ_3) were generated for the three spectral channels. The normalized intensity values were calculated by $I_{1n} = I_1/(I_1 + I_2 + I_3)$, $I_{2n} = I_2/(I_1 + I_2 + I_3)$, and $I_{3n} = I_3/(I_1 + I_2 + I_3)$, where I_1, I_2, and I_3 are the absolute time-integrated intensity values at corresponding pixels in the 390, 452, and >500 nm spectral bands, respectively. The MCP-PMT signal collected at each pixel was 200 ns in duration and contained three consecutive fluorescence decays from the three spectral channels. The measured instrument response function was deconvolved from the measured fluorescence decays using the Laguerre deconvolution method. The average lifetime τ_{ave} was estimated from the deconvolved intrinsic fluorescence decay $h(t)$ as $\tau_{ave} = \sum t \cdot h(t) / \sum h(t)$, where t is time.[34]

For high resolution RCM, a near infrared (NIR) continuous wave diode-pumped solid state laser (1064 nm, 1 W, CL1064-1W0, Crystalaser, Reno, Nevada) was used as the illumination source. A combination of a half-wave plate and a linear polarizer in the beam path served as a variable attenuator to control the optical power incident on the sample. A spatial filter in the beam path was used to produce a clean Gaussian beam. An 8 kHz resonant scanner and a galvanometer scanner operating at 7 Hz (CRS 8K and 6215HM40, Cambridge Technology) were close-coupled to raster scan the NIR beam. A 2× beam expander filled the back aperture of a water immersion 60×, 1.0 NA, 2 mm working distance microscope objective lens (LUMPLFLN60X/W, Olympus, Center Valley, Pennsylvania), which focused the light onto the sample. A combination of linear polarizer, polarizing beamsplitter, and quarter waveplate were used to remove specular reflections within the optical system. Finally, a spatial filter with confocal pinhole of 30 μm diameter for optimized system characterization and 50 μm diameter for tissue imaging rejected out of focus light prior to signal detection by an avalanche photodiode (APD) module (APD110C, Thorlabs). The generated voltage signal was digitized at 39.55 MHz by the digitizer, shared with the FLIM module. Position signals from the scanning mirrors were used as triggers for the confocal data acquisition and image formation. The images were corrected for the nonlinear sinusoidal scan of the resonant scanner and displayed in real-time. To improve contrast for print viewing, RCM images were cropped and contrast-enhanced using ImageJ software (http://imagej.nih.gov/ij/, National Institutes of Health, Bethesda, Maryland).

An automated translation stage was used to move the sample between the FOVs of the FLIM and the RCM subsystems which are approximately 90 mm apart. A paper 1951 United States Air Force (USAF) resolution target (NT53-715, Edmund Optics) with a black pattern printed on a white background and a reflective positive USAF high-resolution target immersed in water (NT58-198, Edmund Optics) were used to measure FOV and lateral resolution of the FLIM and RCM modules, respectively. Confocal axial resolution was measured by translating a planar mirror immersed in water through the focus in 0.5 μm steps and measuring the full width half maximum (FWHM) of the axial point spread function. The relative distance between the centers of the FOV's was also calibrated using a 1951 positive USAF resolution target placed on a white paper and was later used to acquire coregistered images from the two subsystems with lateral accuracy less than the FLIM lateral resolution. The maximum background level in the FLIM system was evaluated by imaging a mirror placed in the FLIM focal plane.

2.2 *Tissue Phantom Preparation and Imaging*

A two-layer tissue phantom was developed to test the system's capability to detect the macroscopic biochemical and microscopic morphological properties of a relatively complex sample. The phantom was produced with a 100 to 120 μm thin top layer consisting of polymer beads to model the epithelial nuclei on a thick lower layer of collagen matrix. This collagen was not fluorescent at 355 nm excitation. NADH and FAD (Sigma-Aldrich, St. Louis, Missouri) were also added to the top layer to represent the respective metabolic coenzymes in the epithelium. The beads together with FAD and NADH were embedded within collagen gel. Collagen gels were first prepared using rat tail tendon type I collagen (BD Biosciences, Franklin Lakes, New Jersey) using the vendor's protocol. Briefly, dissolved collagen was added to 10× phosphate buffered saline (PBS) solution and 1 M sodium hydroxide (NaOH) along with deionized water. The collagen solution can be used immediately or held on ice for 2 to 3 h. For preparation of the top layer, polystyrene microspheres (Bangs Labs, Fishers, Indiana) of 6.15 ± 0.19 μm diameter and concentration of 10% w/w were added to the collagen solution for a final concentration of ~3.5% v/v. NADH and FAD in powdered form were added to achieve final concentration of 1 mmol for each coenzyme. NADH was concentrated towards the center of the phantom and FAD was uniformly distributed throughout the phantom. Finally, the collagen solution was allowed to gel at 37°C for 30 min. The bottom layer was composed of collagen gel only, also nonfluorescent. The tissue phantom samples were prepared in a 96-well plate. The diameter of the wells was measured to be ~7 mm. The FLIM FOV was adjusted accordingly to capture a single well within the image.

2.3 *Oral Mucosa Imaging*

Porcine buccal mucosa is used as a model of human oral mucosa due to their similar epithelial thickness, nuclear size, and cell density. Healthy porcine tissue was obtained from a local slaughterhouse or through the tissue sharing program at Texas A&M University, and transported to the lab for imaging within a couple of hours postmortem. 2×2.5 cm^2 buccal mucosa tissue

samples were excised from the inner cheek and placed in PBS solution prior to imaging. The pig tissue was at room temperature (~70°F) during imaging. After imaging, tissue samples from the imaged locations were obtained, fixed in 10% formalin, and processed for hematoxylin and eosin (H&E) histological comparison.

The hamster cheek pouch model of oral cancer was employed to evaluate *in vivo* imaging of premalignant oral mucosal tissue. Specifically, the hamster was imaged during the early stages of 7, 12-dimethylbenz[α]anthracene (DMBA)-induced oral carcinogenesis. A Golden Syrian hamster was used in this study. The animal use protocol was reviewed and approved by the Texas A&M University Institutional Animal Care and Use Committee (IACUC), and a veterinarian oversaw the clinical aspects of this study. The hamster was housed in pathogen-free conditions and fed with rodent chow and water *ad libitum*. The right buccal pouch of the hamster was treated 3 times a week for 8 weeks with 0.5% solution of DMBA (Sigma-Aldrich) dissolved in mineral oil (Sigma-Aldrich). The left pouch was treated with mineral oil only and served as a normal control. At the time of imaging, the hamster was anesthetized using an intraperitoneal injection of 10% urethane solution. Once anesthetized, the hamster cheek pouch was pulled and clamped into a custom built mount to expose maximum tissue area. During the imaging procedure, the anesthetized hamster was kept warm with a heating pad. The exposed cheek pouch was likely between room temperature and body temperature of the hamster. After imaging of the buccal mucosa, the hamster was euthanized with a solution of pentobarbital. The cheek pouches were then excised, fixed in 10% formalin, and processed for H&E histology.

Samples were first imaged with the FLIM module, then positioned for confocal imaging. Pig and hamster tissue were treated with vinegar (5% acetic acid) for 1 to 2 min following FLIM imaging and prior to RCM imaging. Application of acetic acid results in an increase in scattering by the nuclei, termed acetowhitening, and thereby improves the contrast and the ability to delineate nuclei within the surrounding cytoplasm in RCM imaging.[35,36] Apple cider vinegar has the same acetowhitening effect and has previously been used as a better tasting alternative to white vinegar for *in vivo* confocal imaging of the oral mucosa in humans.[18] The samples were translated in 2 to 3 μm axial steps to acquire three dimensional confocal data. RCM data were acquired at six sites within the pig cheek distributed across the FLIM imaging area. In the DMBA-treated hamster cheek pouch, spatial features in the FLIM intensity and lifetime images were used to guide RCM data acquisition. Fifteen sites were imaged with RCM in the treated pouch, and three sites were imaged in the contralateral normal pouch.

For all samples, the pulse energy of the 355 nm laser was set to be ~1 μJ/pulse which corresponds to an average power of 10 mW at the sample. The maximum illumination power at the sample from the 1064 nm laser was set below 45 mW. These values are below the maximum permissible exposure for skin at the corresponding wavelengths.

One major challenge of validation studies of optical imaging techniques, particularly small FOV imaging, is accurate correlation with histology. The FLIM-RCM system software recorded the mapping coordinates of RCM imaging sites for accurate registration to the FLIM image and for localization relative to the edge of the tissue mount. However, it was very difficult to completely immobilize the approximately 16×16 mm^2 specimens when sectioning them for histologic processing. This could potentially result in some inherent error in coregistration of the imaging sites and the corresponding histology sections, especially for the confocal imaging sites due to the relatively small FOV.

3 Results

3.1 *Optical System Performance*

The RCM-FLIM system was first characterized by imaging fluorescent and reflective USAF resolution targets. The FOV of the FLIM subsystem was set to be 16×16 mm^2 while being able to distinguish element 1 of group 3 corresponding to a lateral resolution of 62.5 μm, as seen in Fig. 2(a), using 400×400 pixels per image and 10 KHz laser repetition rate. A single image acquisition time in the FLIM module takes 19.2 s. The spatial resolution and frame rate of the FLIM subsystem can be adjusted depending on the number of pixels used in a specific FOV and the laser repetition rate; therefore, higher frame rates can be achieved at the expense of lower spatial resolution. The temporal resolution of the FLIM system is calculated to be 320 ps based on the Nyquist theorem. The background signal was characterized under worst-case conditions by imaging a mirror placed at the focal plane of the FLIM system. The signal level detected was less than 10% of the level detected in tissue samples at equivalent detector gain conditions. In addition, the lifetime of the background signal was found to be less than 1 ns, confirming that it corresponds to the reflected excitation light reaching the detector and not to autofluorescence within the optical system. The background level is expected to be much weaker when imaging a low-reflectance sample such as tissue. The RCM system was measured to have a 400 μm diameter FOV [Fig. 2(b)] and a lateral resolution of 0.97 μm or less, based on resolution of element 1 of group 9 [Fig. 2(c)]. The FWHM axial resolution was measured to be 3.5 and 4.5 μm using 30 and 50 μm diameter pinholes, respectively. The larger pinhole was used for imaging tissue samples to increase signal to noise ratio.

3.2 *Tissue Phantom Imaging*

The performance of the RCM-FLIM system was further evaluated by imaging the two-layer phantom. Since the collagen gel that was used for embedding the NADH, FAD, and particles was found to be nonfluorescent at 355 nm excitation, the signal in the 390 nm channel was less than 5% relative to the 452 nm and

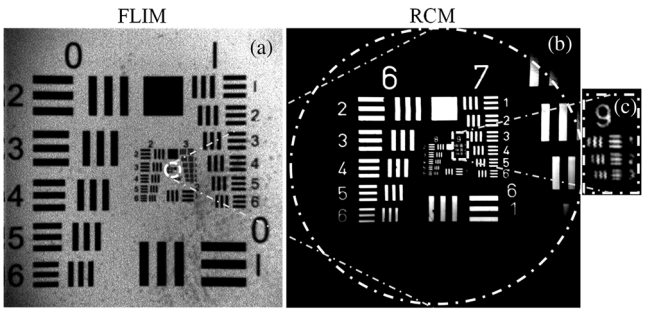

Fig. 2 (a) 16×16 mm^2 FLIM image of fluorescent positive United States Air Force (USAF) target. Element 1 of group 3, corresponding to a line width of 62.5 μm, can be resolved. (b) 400 μm diameter (dashed circle) RCM image of positive USAF target. Outlined region in (a) provides relative scale of the FLIM and RCM modalities. (c) Zoom in of group 9 in (b). Element 1, corresponding to a line width of 0.97 μm, is resolvable.

>500 nm channels. Therefore, images are shown only for the 452 nm [Fig. 3(a) and 3(c)] and >500 nm [Fig. 3(b) and 3(d)] bands corresponding to NADH and FAD emission, respectively. The circular mask shown in Fig. 3(a) to 3(d) is the boundary of the phantom well in the 96-well plate. At 355 nm excitation, peak emission wavelengths for NADH and FAD are around 450 and 520 nm, respectively. A small amount of NADH fluorescence signal may be detected in the FAD band, whereas FAD fluorescence is limited to the >500 nm band. Figure 3(a) and 3(b) shows FLIM normalized intensity maps at 452 and >500 nm. The center of the phantom, where both NADH and FAD are present, provided fluorescence signal in both of the spectral channels (0.48 ± 0.08 a.u. in 452 nm band, and 0.45 ± 0.08 a.u. in >500 nm band). At the periphery of the phantom, the overall signal was dominated by FAD fluorescence in the >500 nm spectral channel (0.88 ± 0.09 a.u.). The known average lifetimes for unbound NADH and FAD are approximately

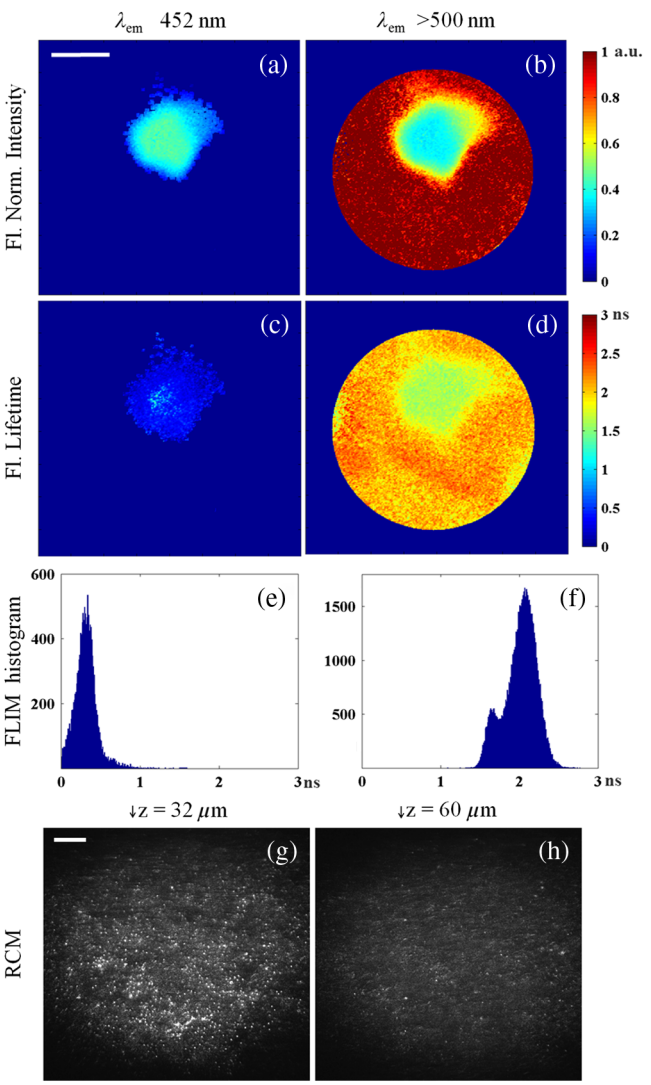

Fig. 3 FLIM-RCM images of the two-layer phantom. FLIM normalized intensity maps at spectral bands of (a) 452 nm and (b) >500 nm, and FLIM average lifetime maps and histograms at (c) and (e) 452 nm and (d) and (f) >500 nm, respectively. RCM images taken at (g) 32 μm and (h) 60 μm depths. Polymer beads are visible as bright spots within the surrounding medium. Scale bars: (a) 2 mm for FLIM and (e) 50 μm for RCM.

0.5 ns and 2 to 2.5 ns, respectively.[33] Figure 3(c) and 3(d) is the average lifetime maps, and Fig. 3(e) and 3(f) are the corresponding lifetime histograms. As shown in the figures, the average lifetime for the center of the phantom in the 452 nm channel is 0.32 ± 0.15 ns corresponding to the lifetime of NADH. The average lifetime in the >500 nm channel is 2.08 ± 0.15 ns at the periphery which represents FAD, and 1.72 ± 0.14 ns in the center due to the combination of NADH and FAD signal.

Figure 3(g) and 3(h) shows the confocal images from the top-layer of the tissue phantom, at depths of approximately 30 and 60 μm, respectively. The polystyrene beads appeared as white dots in the reflectance images, and were fairly uniformly distributed over the entire FOV. The thickness of the top-layer was measured to be 120 μm by scanning the sample axially with the RCM module using 3 μm step size. For the purpose of RCM, the ~6 μm diameter beads' appearance was similar to that of cell nuclei. The collagen gel provided additional background scattering similar to tissue. The relative brightness of the beads in comparison to cell nuclei (shown later below) was high due to the significant back-scattering component associated with the large relative refractive index of beads inside the collagen gel.[37] These results demonstrate that such a two-layer phantom is well-suited to validate our dual-modality imaging system.

3.3 *Porcine Buccal Mucosa Imaging Ex Vivo*

Multispectral FLIM results of normal pig buccal mucosa tissue are shown in Fig. 4(a) to 4(f). The normalized intensity maps [Fig. 4(a) to 4(c)] indicate slightly stronger fluorescence signal in the 452 nm band (0.42 ± 0.02 a.u.), followed by the >500 nm band (0.31 ± 0.03 a.u.), and the 390 nm band (0.27 ± 0.02 a.u.). The weak signal in the collagen channel may be due to the thick epithelium which makes it difficult for the fluorescence from collagen to reach the surface of the tissue. The thickness of the epithelium is more than 400 μm, as shown in the H&E histology images in Fig. 4(j). The average lifetime images [Fig. 4(d) to 4(f)] showed relatively longer values at 390 nm (5.84 ± 0.49 ns), followed by >500 nm (5.09 ± 0.41 ns) and 452 nm (4.26 ± 0.41 ns) channels. Both intensity and lifetime maps are homogeneous, as expected in normal tissue.

The RCM images in Fig. 4(g) to 4(i) clearly show the epithelial cell nuclei as bright spots on a darker background. The media file shows RCM video as the image plane is translated from the tissue surface to 300 μm in depth (Video 1). Both the nuclear density and nuclear-to-cytoplasmic ratio increased with depth in the epithelium, which is a hallmark of normal epithelium. Cell nuclei were detectable in RCM images down to a depth of 300 μm below the surface. Figure 4(j) shows an H&E histology image of a tissue sample taken from the region imaged. The size and spatial distribution of nuclei in the *en face* confocal images correlates well with the cross-sectional histology image.

3.4 *Precancerous Hamster Cheek Pouch Imaging In Vivo*

Figure 5 shows multispectral FLIM, RCM, H&E histology, and photograph images of normal [Fig. 5(a) to 5(k)] and precancerous hamster cheek pouch treated with DMBA carcinogen [Fig. 5(l) to 5(z)]. Histopathological diagnoses of sections spanning the entire imaging area in the treated pouch include normal,

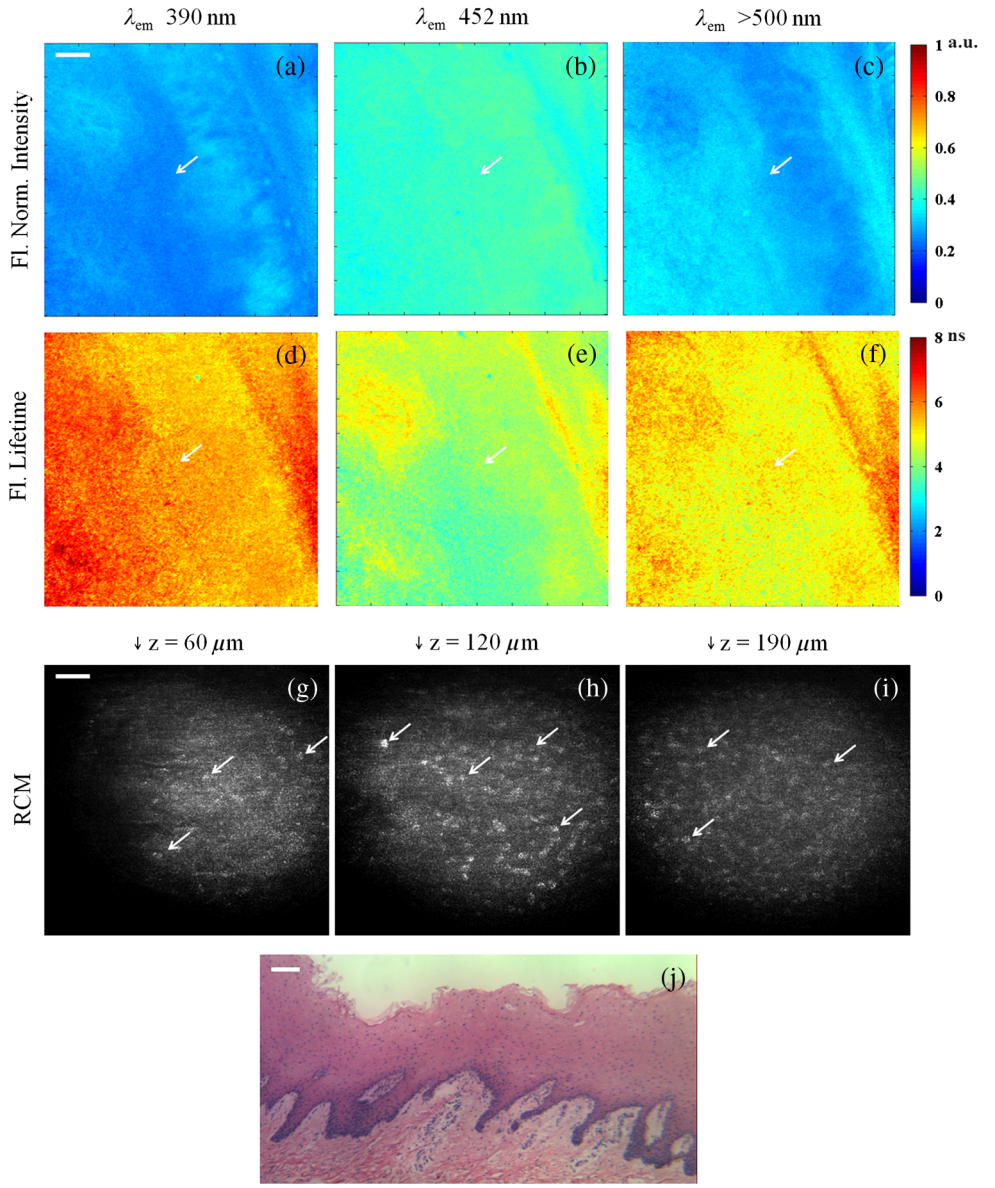

Fig. 4 *Ex vivo* FLIM-RCM images of normal porcine buccal mucosa. FLIM normalized intensity maps at (a) 390 nm, (b) 452 nm, and (c) >500 nm. FLIM average lifetime maps at (d) 390 nm, (e) 452 nm, and (f) >500 nm. Arrows identify the RCM imaging location at the center of the FLIM FOV. RCM images obtained at (g) 60 μm, (h) 120 μm, and (i) 190 μm depths. The corresponding video shows RCM images scanning from the surface down in depth to 300 μm (Video 1). Arrows point to individual nuclei. (j) 10× H&E histology image of tissue. Scale bars: (a) 2 mm, (g) 50 μm, and (k) 100 μm. (Video 1, QuickTime, 3.3 MB) [URL: http://dx.doi.org/10.1117/1.JBO.18.4.046012.1].

cytologic atypia, low-grade dysplasia, high-grade dysplasia, and cancer [papillary tumor in the lower right quadrant of Fig. 5(r)].

Figure 5(a) to 5(f) shows the normalized fluorescence intensity and average lifetime maps for the normal hamster cheek pouch. The normalized fluorescence intensity values were 0.42 ± 0.04 a.u., 0.3 ± 0.01 a.u., and 0.28 ± 0.03 a.u., and lifetimes values were 5.61 ± 0.13 ns, 4.06 ± 0.25 ns, and 4.22 ± 0.29 ns for the 390 nm, 452 nm, and >500 nm bands, respectively. For the specific RCM-imaged region in the center of the FLIM FOV, the normalized intensity values were 0.41 ± 0.01 a.u., 0.31 ± 0.01 a.u., and 0.28 ± 0.01 a.u., and lifetimes values were 5.67 ± 0.08 ns, 4.67 ± 0.11 ns, and 4.34 ± 0.13 ns for the 390 nm, 452 nm, and >500 nm bands, respectively. These results are consistent with a dominant collagen fluorescence emission that peaks at 390 nm and has an average lifetime around 5 to 6 ns. This is expected for the normal hamster cheek pouch, since the epithelium is very thin [Fig. 5(k)] and most of the autofluorescence emission should come from collagen in the connective tissue. In comparison to the weak collagen signal in the thick porcine buccal mucosa, the fluorescence intensity in the 390 nm band was relatively high in the hamster cheek pouch tissue due to the very thin epithelium. The RCM images taken from the center of the FLIM FOV at approximate depths of 18 μm [Fig. 5(h)] and 39 μm [Fig. 5(i)] show scattering from the keratin at the surface and epithelial nuclei beneath this superficial layer. Figure 5(j) is a zoomed in view of Fig. 5(i) to more clearly show the cell membranes and nuclei identified by arrows.

Figure 5(l) to 5(q) shows the normalized fluorescence intensity and average lifetime maps for the DMBA-treated hamster cheek pouch. As seen in the corresponding photograph of the tissue in Fig. 5(r) and in the FLIM images, a tumor is visible

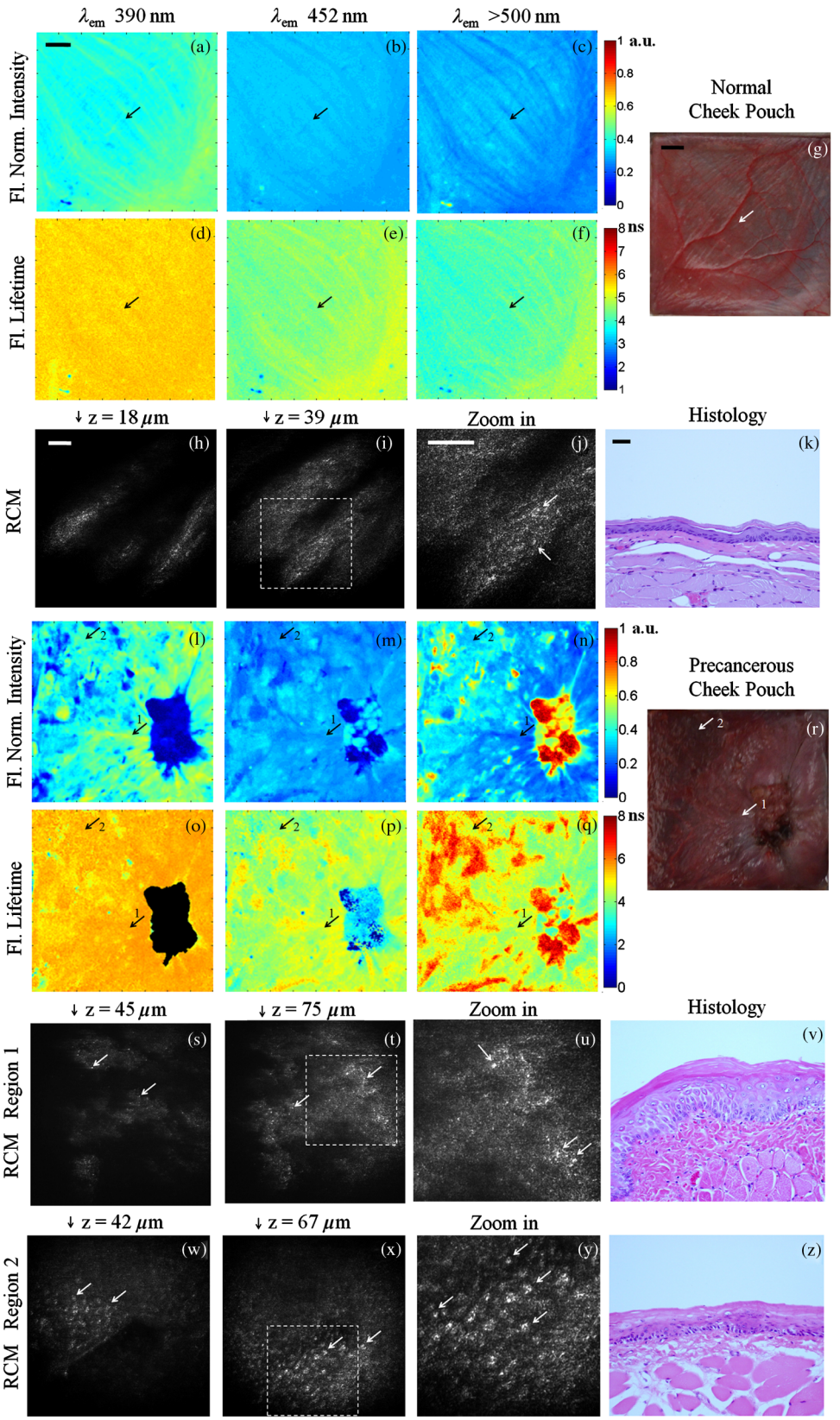

Fig. 5 *In vivo* FLIM-RCM images of (a) to (k) normal and (l) to (z) DMBA-treated hamster cheek pouch. Normalized FLIM intensity maps at (a) and (l) 390 nm, (b) and (m) 452 nm, and (c) and (n) >500 nm spectral bands. FLIM average lifetime maps at (d) and (o) 390 nm, (e) and (p) 452 nm, and (f) and (q) >500 nm spectral bands. (g) and (r) Photographs of FLIM imaging areas. Arrows in FLIM and photo images correspond to regions for subsequent RCM images. Arrows labeled 1 and 2 in (l) to (r) correspond to regions 1 [(s) to (v); cytologic atypia] and 2 [(w) to (z); low-grade dysplasia], respectively. RCM images (h), (i), (s), (t), (w), and (x) taken at indicated depths. Zoom in RCM images (j), (u), and (y) taken from dotted squares in (i), (t), and (x), respectively. Arrows in RCM images indicate nuclear features. Corresponding video shows RCM images scanning in depth in region 2 (Video 2). (k), (v), and (z) 25× H&E histology images from RCM regions. Scale bars: (a) and (g) 2 mm, and (h), (j), and (k) 50 μm. (Video 2, QuickTime, 1.0 MB) [URL: http://dx.doi.org/10.1117/1.JBO.18.4.046012.2].

in the lower right quadrant of the tissue. RCM imaging was performed in a number of locations throughout the cheek pouch, two of which are identified by arrows labeled "1" and "2" in the FLIM images. Region 1 was later diagnosed as cytologic atypia [Fig. 5(v)] and region 2 was diagnosed as low-grade dysplasia [Fig. 5(z)] by histopathology. In these lesions, the fluorescence lifetime in the 452 nm channel was shorter (4.32 ± 0.18 ns and 4.29 ± 0.29 ns in regions 1 and 2, respectively) compared to the normal tissue (>5 ns). The epithelium is thicker than the normal epithelium, thus the fluorescence emission is generated both from NADH in the epithelium and from collagen in the connective tissue, although the collagen fluorescence is still dominant. Since NADH has a much shorter fluorescence lifetime (~0.5 to 2 ns) and its peak emission is at 450 nm, the resulting fluorescence in the precancerous lesions is expected to have shorter lifetimes at 452 nm than in normal tissue. The RCM images of region 1 just below the surface [Fig. 5(s)] and deeper in the epithelium [Fig. 5(t) and Fig. 5(u) zoomed in] show very small features that may be epithelial nuclei or possibly nucleoli that can be seen in the corresponding histology section in Fig. 5(v). In contrast, the RCM images of the epithelium in region 2, shown in Fig. 5(w) and 5(x) and Fig. 5(y) zoomed in, show much larger nuclei indicative of precancerous changes. Arrows in RCM images identify cell nuclei. These results illustrate that RCM allows identification of cellular changes from two pathologically different regions in areas that look abnormal but similar based on FLIM imaging.

In the tumor region, the epithelium is so thick that all the fluorescence contribution is coming from this layer. Since the collagen in the connective tissue is no longer excited, the signal at 390 nm was insignificant (0.06 ± 0.03 a.u.). Strong emission was observed at >500 nm (0.75 ± 0.14 a.u.) and significant emission was also observed at 452 nm (0.19 ± 0.11 a.u.). The extremely low 390 nm signal in the tumor resulted in inaccurate lifetime measurements; therefore, the lifetime map in Fig. 5(d) is masked in this region. The fluorescence lifetime at 452 nm was much shorter (2.62 ± 0.79 ns) compared to normal and precancerous tissue indicating a greater fluorescence contribution from NADH. The fluorescence lifetime in the 500 nm channel was longer (5.62 ± 1.27 ns) compared to normal and precancerous tissue indicating contribution of both FAD and porphyrin; porphryin has relatively long lifetime (>6 ns). All the FLIM results are summarized in Table 1 and are consistent with similar systems reported in Ref. 38.

4 Discussion

This work shows that our dual-modality multispectral FLIM and RCM imaging system can effectively image biochemical and morphological features in tissue. While large-FOV FLIM enables fast macroscopic tissue evaluation in the above described implementation, it lacks the ability to provide optical sectioning and high spatial resolution for cellular evaluation. The RCM subsystem can provide much higher spatial resolution and optical sectioning necessary for cellular imaging but has a limited FOV. The combination of these imaging techniques on a single platform offers an important and powerful tool built upon the strengths of the individual subsystems. The complementary information acquired from the integration of the two modalities is important for the study of biological changes such as seen in the progression of early cancer.

In all instances, FLIM imaging provided macroscopic biochemical maps which represent the relative contribution of the endogenous fluorophores, both with respect to fluorescence intensity and lifetime. While the FLIM images of the tissue phantom showed some physical features due to the geometry of the phantom and the distribution of NADH and FAD, the images of the biological samples showed differences in intensity and lifetime signals between normal and cancer. The FLIM maps of healthy pig mucosa were relatively homogeneous, as expected, due to the uniform nature of the normal tissue. The detected collagen signal from the pig mucosa with thick epithelium and the clear nuclei seen with RCM at different depths of tissue demonstrate the potential for translation to human oral tissue. Normal human oral mucosa, with an epithelial thickness ranging from 190 to 580 μm depending on the site in the oral cavity and cell nuclear diameters on the order of 10 μm, has similar tissue architecture and cell morphology to pig oral mucosa.[39] In comparison, the hamster tissue had a wide range of pathologies, resulting in spatial features in both the intensity and lifetime images. Additionally, the spectral and lifetime data

Table 1 Normalized fluorescence intensities (a.u.) and average lifetimes (ns) from FLIM imaging of center (NADH/FAD) and periphery (FAD) of phantom (no collagen fluorescence); normal porcine mucosa; normal hamster cheek pouch and RCM imaging region; and tumor region, RCM region 1 (cytologic atypia), and RCM region 2 (low-grade dysplasia) of DMBA-treated hamster cheek pouch.

		390 nm		452 nm		>500 nm	
Sample	λ_{em} Channels	Intensity	Lifetime	Intensity	Lifetime	Intensity	Lifetime
Phantom	Center	—		0.48 ± 0.08	0.32 ± 0.15	0.45 ± 0.08	1.72 ± 0.14
	Periphery	—		—		0.88 ± 0.09	2.08 ± 0.15
Normal pig	Entire FOV	0.27 ± 0.02	5.84 ± 0.49	0.42 ± 0.02	4.26 ± 0.41	0.31 ± 0.03	5.09 ± 0.41
Normal hamster	Entire FOV	0.42 ± 0.04	5.61 ± 0.13	0.30 ± 0.01	4.60 ± 0.25	0.28 ± 0.03	4.22 ± 0.29
	RCM region	0.41 ± 0.01	5.67 ± 0.08	0.31 ± 0.01	4.67 ± 0.11	0.28 ± 0.01	4.34 ± 0.13
DMBA-treated hamster	Tumor	0.06 ± 0.03	5.43 ± 0.14	0.19 ± 0.11	2.62 ± 0.79	0.75 ± 0.14	5.62 ± 1.27
	RCM region 1	0.49 ± 0.02	5.49 ± 0.16	0.28 ± 0.01	4.32 ± 0.18	0.23 ± 0.02	4.23 ± 0.21
	RCM region 2	0.42 ± 0.02	5.43 ± 0.14	0.27 ± 0.01	4.29 ± 0.29	0.30 ± 0.01	5.16 ± 0.34

of the DMBA-treated pouch was different than the normal control pouch, indicating the ability to detect precancerous changes. By comparing normalized intensity and average lifetime values in Table 1, differentiation between normal and tumorous tissue may be achieved with intensity measurements alone. However, based on some similarity in normalized intensity values and differences in lifetimes between normal tissue and the DMBA-treated RCM regions 1 and 2, the more challenging and relevant problem of distinguishing between benign and precancerous lesions may be realized with FLIM. It should be noted that the histopathological difference between the normal and precancerous lesions being compared were very subtle; yet, difference in the FLIM signal could already be observed. Nevertheless, the high resolution of RCM was still necessary for identifying cellular changes indicative of precancer.

The results from the high-resolution RCM demonstrate the potential of the imaging system towards characterization of subcellular morphological features of the epithelial tissue. The brighter nuclei against the darker background can be delineated in the RCM images and videos. The normal cell nuclei in the porcine tissue are on the same scale as normal human epithelial cell nuclei. Although normal hamster epithelial nuclei are smaller, they are still detectable with our RCM imaging system. An increase in nuclear size was distinguished between normal and dysplastic tissue in hamster cheek pouch. RCM images of epithelial nuclei can be further analyzed either manually or through automated image processing to calculate more objective parameters defining epithelial tissue characteristics such as nuclear size, nuclear density, and nuclear-to-cytoplasmic ratio.[40] The RCM system was able to distinguish between two pathologically different regions that look the same (abnormal) using FLIM. This shows the importance of these two complementary techniques. The aim of this study is to use FLIM as a more sensitive guide while the RCM may provide a more specific diagnostic.

A single image acquisition through our current embodiment of FLIM generated large amount of data, considering a single set of FLIM images was 400×400 pixels and each pixel carries time-multiplexed information related to three spectral bands. The resultant images were processed in MATLAB which is very flexible but does not offer fast execution speeds being an interpreted language. Such a limitation can potentially be avoided by processing the images using a compiled programming language and/or field-programmable gate arrays (FPGA). Using a FPGA device can allow us to circumvent the inherent delay associated with software and control of computer-programmable devices in the personal computing environment.

It is worth comparing our system to other optical microscopes or endoscopes previously investigated in research for cancer detection. All of our FLIM data are taken from wide-field FLIM images (16×16 mm^2) of epithelium and stroma of bulk tissue. These results will not directly correspond to small FOV multiphoton FLIM of only epithelium, for example. *In vivo* multiphoton FLIM measurements of the lifetime values in epithelium have been reported,[32,41,42] and this technology has been translated to a clinical device (Jenlab, DermaInspect and MPTFlex).[43,44] While this technique has the advantage of biochemical and morphological imaging with optical sectioning, the main disadvantages of such systems are the need for macroscopic guidance and the significant cost compared to RCM. Confocal fluorescence endoscopy and microendoscopy has been explored extensively using both endogenous and exogenous contrast. As we have mentioned, intensity based fluorescence imaging can be confounded by the overlapping spectral properties of the biochemicals of interest.[12,20] To circumvent the limited FOV of RCM imaging, the Lucid Vivascope, a clinical device for dermatologic imaging *in vivo* and *ex vivo*, uses mosaicing of microscopic images acquired using a step-and-capture technique.[45,46] Although speed enhancements have increased acquisition speed for confocal pathology of tissue specimens,[47] image mosaicing is typically limited to a single depth and large area imaging is quite time consuming. Mosaicing has also been successfully applied to other confocal microendoscopy applications indicating the potential for expanded FOV with high resolution RCM;[48] however, screening of entire organs using high resolution imaging still remains impractical. There are a number of optical techniques with various permutations of biochemical imaging, morphological imaging, optical sectioning, at a range of scales and resolutions to detect precancerous changes in tissue. In our approach, we achieve a rapid large-area screening of metabolic changes in tissue followed by morphological evaluation akin to histopathology.

5 Conclusion

In summary, we have presented the design and development of a dual-modality multiscale FLIM-RCM imaging system applied to the characterization of oral epithelial tissue. The integrated system is capable of identifying both morphological features and the biochemical composition of mucosal tissue, which together can potentially serve as a powerful diagnostic aid towards classification of pathological condition of the tissue. Such a simultaneous characterization of tissue physiology may be used to assess if the sample is normal, benign, premalignant or malignant, and may ultimately be used as a guiding tool for standard screening and intervention methods.

We are currently evaluating the system described here for differentiation of precancer from benign lesions in the hamster cheek pouch model. Following validation of the technology in an animal model and in human biopsies, the system can be miniaturized for *in vivo* imaging in humans using lens relays, fiber bundles, and miniature lenses.[18,49,50] The implementation may include a single integrated probe or two separate imaging probes.

Acknowledgments

This research was supported by National Institutes of Health (R01CA138653). The authors would like to thank Dr. Vincent Gresham and Kelsey Johnson from the Comparative Medicine Program at Texas A&M University for their help with anesthesia and euthanesia protocol for the hamster experiment, Meagan Saldua and Astride Tchoffo for assistance with optics alignment, and Carl Johnson for machining the hamster cheek pouch mount.

References

1. Training SEER Modules, "Cancer as a disease," National Cancer Institute. U.S. National Institutes of Health, http://training.seer.cancer.gov/ (24 December 2012).
2. American Cancer Society, *Cancer Facts & Figures 2012*, American Cancer Society, Atlanta, Georgia (2012).
3. P. Wilder-Smith et al., "In vivo diagnosis of oral dysplasia and malignancy using optical coherence tomography: preliminary studies in 50 Patients," *Lasers Surg. Med.* **41**(5), 353–357 (2009).

4. T. J. Muldoon et al., "Noninvasive imaging of oral neoplasia with a high-resolution fiber-optic microendoscope," *Head Neck* **9999**(9999), 1–8 (2011).
5. B. Larson, S. Abeytunge, and M. Rajadhyaksha, "Performance of full-pupil line-scanning reflectance confocal microscopy in human skin and oral mucosa in vivo," *Biomed. Opt. Express* **2**(7), 2055–2067 (2011).
6. B. Farahati et al., "Rigid confocal endoscopy for in vivo imaging of experimental oral squamous intra-epithelial lesions," *J. Oral Pathol. Med.* **39**(4), 318–327 (2010).
7. J. Sun et al., "In vivo multimodal nonlinear optical imaging of mucosal tissue," *Opt. Express* **12**(11), 2478–2486 (2004).
8. B. R. Haxel et al., "Confocal endomicroscopy: a novel application for imaging of oral and oropharyngeal mucosa in human," *Eur. Arch. Oto Rhino Laryngol.* **267**(3), 443–448 (2010).
9. D. Roblyer et al., "Objective detection and delineation of oral neoplasia using autofluorescence imaging," *Cancer Prev. Res.* **2**(5), 423–431 (2009).
10. A. Gillenwater, V. Papadimitrakopoulou, and R. Richards-Kortum, "Oral premalignancy: new methods of detection and treatment," *Curr. Oncol. Rep.* **8**(2), 146–154 (2006).
11. J. A. Jo et al., "In vivo simultaneous morphological and biochemical optical imaging of oral epithelial cancer," *IEEE Trans. Biomed. Eng.* **57**(10), 2596–2599 (2010).
12. J. M. Jabbour et al., "Confocal endomicroscopy: instrumentation and medical applications," *Ann. Biomed. Eng.* **40**(2), 378–397 (2012).
13. W. M. White et al., "Noninvasive imaging of human oral mucosa in vivo by confocal reflectance microscopy," *Laryngoscope* **109**(10), 1709–1717 (1999).
14. S. Inoué, "Foundations of confocal scanned imaging in light microscopy," Chapter 1, in *Handbook of Biological Confocal Microscopy*, J. B. Pawley, Ed., pp. 1–19, Springer, New York (2006).
15. A. K. Dunn et al., "Sources of contrast in confocal reflectance imaging," *Appl. Opt.* **35**(19), 3441–3446 (1996).
16. J. J. Pindborg et al., *Histological Typing of Cancer and Precancer of the Oral Mucosa*, Springer, Berlin (1997).
17. B. W. Neville, *Oral & Maxillofacial Pathology*, Saunders/Elsevier, St. Louis, Missouri (2009).
18. K. C. Maitland et al., "In vivo imaging of oral neoplasia using a miniaturized fiber optic confocal reflectance microscope," *Oral Oncol.* **44**(11), 1059–1066 (2008).
19. A. L. Clark et al., "Detection and diagnosis of oral neoplasia with an optical coherence microscope," *J. Biomed. Opt.* **9**(6), 1271–1280 (2004).
20. M. Olivo, R. Bhuvaneswari, and I. Keogh, "Advances in bio-optical imaging for the diagnosis of early oral cancer," *Pharmaceutics* **3**(3), 354–378 (2011).
21. Y. C. Ahn et al., "Multimodality approach to optical early detection and mapping of oral neoplasia," *J. Biomed. Opt.* **16**(7), 076007 (2011).
22. M. C. Pierce et al., "Wide-field and high-resolution optical imaging for early detection of oral neoplasia," *Proc. SPIE* **7548**, 75481U (2010).
23. R. Patel et al., "Multimodal optical imaging for detecting breast cancer," *J. Biomed. Opt.* **17**(6), 066008 (2012).
24. J. B. Epstein et al., "Analysis of oral lesion biopsies identified and evaluated by visual examination, chemiluminescence and toluidine blue," *Oral Oncol.* **44**(6), 538–544 (2008).
25. K. H. Awan, P. R. Morgan, and S. Warnakulasuriya, "Evaluation of an autofluorescence based imaging system (VELscope (TM)) in the detection of oral potentially malignant disorders and benign keratoses," *Oral Oncol.* **47**(4), 274–277 (2011).
26. M. W. Lingen et al., "Critical evaluation of diagnostic aids for the detection of oral cancer," *Oral Oncol.* **44**(1), 10–22 (2008).
27. D. C. De Veld et al., "The status of in vivo autofluorescence spectroscopy and imaging for oral oncology," *Oral Oncol.* **41**(2), 117–131 (2005).
28. I. Pavlova et al., "Understanding the biological basis of autofluorescence imaging for oral cancer detection: high-resolution fluorescence microscopy in viable tissue," *Clin. Cancer Res.* **14**(8), 2396–2404 (2008).
29. P. M. Lane et al., "Simple device for the direct visualization of oral-cavity tissue fluorescence," *J. Biomed. Opt.* **11**(2), 024006 (2006).
30. N. P. Galletly et al., "Fluorescence lifetime imaging distinguishes basal cell carcinoma from surrounding uninvolved skin," *Br. J. Dermatol.* **159**(1), 152–161 (2008).
31. V. K. Ramanujan et al., "Multiphoton fluorescence lifetime contrast in deep tissue imaging: prospects in redox imaging and disease diagnosis," *J. Biomed. Opt.* **10**(5), 051407 (2005).
32. M. C. Skala et al., "In vivo multiphoton fluorescence lifetime imaging of protein-bound and free nicotinamide adenine dinucleotide in normal and precancerous epithelia," *J. Biomed. Opt.* **12**(2), 024014 (2007).
33. S. Shrestha et al., "High-speed multispectral fluorescence lifetime imaging implementation for in vivo applications," *Opt. Lett.* **35**(15), 2558–2560 (2010).
34. P. Pande and J. A. Jo, "Automated analysis of fluorescence lifetime imaging microscopy (FLIM) data based on the Laguerre deconvolution method," *IEEE Trans. Biomed. Eng.* **58**(1), 172–181 (2011).
35. R. A. Drezek et al., "Laser scanning confocal microscopy of cervical tissue before and after application of acetic acid," *Am. J. Obstet. Gynecol.* **182**(5), 1135–1139 (2000).
36. A. F. Zuluaga et al., "Contrast agents for confocal microscopy: how simple chemicals affect confocal images of normal and cancer cells in suspension," *J. Biomed. Opt.* **7**(3), 398–403 (2002).
37. L. Nieman et al., "Optical sectioning using a fiber probe with an angled illumination-collection geometry: evaluation in engineered tissue phantoms," *Appl. Opt.* **43**(6), 1308–1319 (2004).
38. Y. Sun et al., "In vivo validation of a bimodal technique combining time-resolved fluorescence spectroscopy and ultrasonic backscatter microscopy for diagnosis of oral carcinoma," *J. Biomed. Opt.* **17**(11), 116003 (2012).
39. M. J. Rathbone, ed., *Oral Mucosal Drug Delivery*, Marcel Dekker, Inc., New York (1996).
40. B. L. Luck et al., "An image model and segmentation algorithm for reflectance confocal images of in vivo cervical tissue," *IEEE Trans. Image Process.* **14**(9), 1265–1276 (2005).
41. A. J. Walsh et al., "Ex vivo optical metabolic measurements from cultured tissue reflect in vivo tissue status," *J. Biomed. Opt.* **17**(11), 116015 (2012).
42. A. A. Heikal, "Intracellular coenzymes as natural biomarkers for metabolic activities and mitochondrial anomalies," *Biomark Med.* **4**(2), 241–263 (2010).
43. MPTFlex, JenLab, http://www.jenlab.de/MPTflex.114.0.html (26 February 2013).
44. DermaInspect, JenLab, http://www.jenlab.de/DermaInspect-R.29.0.html (26 February 2013).
45. Y. G. Patel et al., "Confocal reflectance mosaicing of basal cell carcinomas in Mohs surgical skin excisions," *J. Biomed. Opt.* **12**(3), 034027 (2007).
46. Lucid Vivascope, http://www.caliberid.com/ (26 February 2013).
47. S. Abeytunge et al., "Rapid confocal imaging of large areas of excised tissue with strip mosaicing," *J. Biomed. Opt.* **16**(5), 050504 (2011).
48. V. Becker et al., "High-resolution miniprobe-based confocal microscopy in combination with video mosaicing (with video)," *Gastrointest. Endosc.* **66**(5), 1001–1007 (2007).
49. K. Carlson et al., "In vivo fiber-optic confocal reflectance microscope with an injection-molded plastic miniature objective lens," *Appl. Opt.* **44**(10), 1792–1797 (2005).
50. S. Cheng et al., "Compact endoscope for in vivo simultaneous multispectral fluorescence lifetime imaging," *Opt. Lett.* (2013) (in press).